Are Hydrodynamic Interactions Important in the Kinetics of Hydrophobic Collapse?

Jingyuan Li,[†,‡] Joseph A. Morrone,[†] and B. J. Berne*[,†]

[†]Department of Chemistry, Columbia University, 3000 Broadway, MC 3103, New York, New York 10027, United States
[‡]Chinese Academy of Sciences Key Lab for Biomedical Effects of Nanomaterials and Nanosafety, Institute of High Energy Physics, Chinese Academy of Sciences, Beijing 100049, China

ABSTRACT: We study the kinetics of assembly of two plates of varying hydrophobicity, including cases where drying occurs and water strongly solvates the plate surfaces. The potential of mean force and molecular-scale hydrodynamics are computed from molecular dynamics simulations in explicit solvent as a function of particle separation. In agreement with our recent work on nanospheres [*J. Phys. Chem. B* **2012**, *116*, 378−389], regions of high friction are found to be engendered by large and slow solvent fluctuations. These slow fluctuations can be due to either drying or confinement. The mean first passage times for assembly are computed by means of molecular dynamics simulations in explicit solvent and by Brownian dynamics simulations along the reaction path. Brownian dynamics makes use of the potential of mean force and hydrodynamic profile that we determined. Surprisingly, we find reasonable agreement between full-scale molecular dynamics and Brownian dynamics, despite the role of slow solvent relaxation in the assembly process. We found that molecular-scale hydrodynamic interactions are essential in describing the kinetics of assembly.
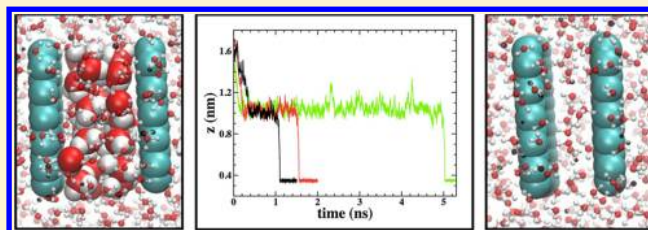
1. INTRODUCTION

Hydrophobic interactions are important in structural biology and nanoscience where they are often the major driving force in self-assembly.[1−9] For example, hydrophobic interactions are acknowledged to play a major role in the formation and folding of proteins.[10,11] A classic example of hydrophobic assembly is that when two plates that bear little attraction to water are separated by less than some critical separation capillary evaporation occurs in the interplate region, thereby driving association.

Although a great deal of work has concentrated on the structural and thermodynamic aspects of hydrophobic assembly, less is known about the kinetic mechanisms involved in the association process. Prior studies have investigated the rate of evaporation of solvent confined between two hydrophobic surfaces,[6,12−15] although the full association pathway remains largely unexplored. One possible route to modeling the kinetics is within the framework of Brownian (Smoluchowski) dynamics, a coarse-grained description in which the solvent degrees of freedom are not explicitly treated and where the dynamics of the heavy bodies are instead modeled in a stochastic bath. The effect of solvent is encoded in the potential of mean force (PMF) between bodies and the friction coefficient. If hydrodynamic interactions (HI) are included, then the friction coefficients depend on the positions of the heavy bodies. Within this framework, one can simulate protein diffusion and association using the appropriate equations together with the potential of mean force and the (position-dependent) friction tensor as input.[16] For example, such an approach has been utilized to study crowded cellular environments, where the diffusion of proteins is thought to slow down considerably due in part to hydrodynamic interactions.[17]

Most typically, hydrodynamic interactions that are utilized in Brownian dynamics simulation are computed within a continuum description of the solvent.[18,19] This description, however, breaks down for interparticle length scales of 1−2 nm.[20,21] On such length scales, fluctuations which accompany solvent layering or capillary drying could have an enormous effect on hydrodynamic interactions. In recent work, we have shown how the nature of solvent confined between nanoscopic spheres determines the role of HI in assembly.[22] There is a growing interest in the behavior of water molecules in confined geometries.[23−25] The diffusion constant and the hydrogen bond lifetime of water molecules in confined environments are distinct from those in the bulk.[26] Furthermore, similar signatures have been recently observed in simulations of crowded protein solutions.[27] We believe such effects can potentially play an important role in the transport and association of nanoscopic bodies.

In this paper, we extend our previous study of nanospheres to the study of hydrodynamic interactions and association kinetics of plates of varying hydrophobicity. We calculate the friction on two parallel plates as a function of their separation from molecular dynamic simulations with explicit water using a technique previously employed for spherical solutes.[22,28] We also calculate the potential of mean force between the two
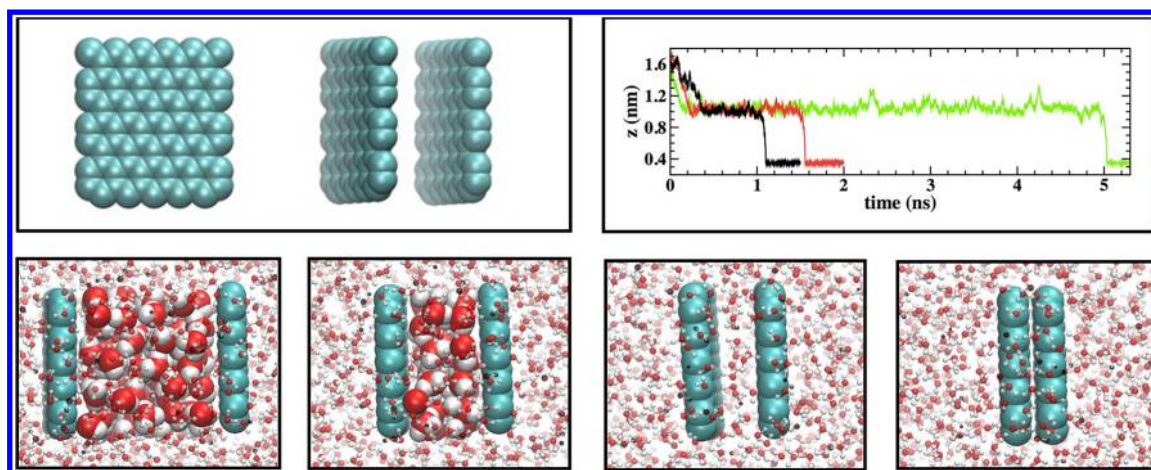
Figure 1. (Upper left panel) Top view and side view of two parallel graphene-like plates. (Upper right panel) Representative association trajectories of two plates with the "reduced" LJ interaction. (Lower panels) Configurations taken from the association of the reduced LJ plates, corresponding to an interplate separation of (from left to right): $z = 1.7$ nm (initial configuration), 1.0 nm (where the association stagnates), 0.7 nm (during the driving induced collapse), and 0.35 nm (when the plates come into contact). The plates and water molecules in the interplate region are depicted by a space-filling representation, and the snapshots are rendered with VMD.[45]

plates as a function of their separation. Both the molecular-scale effects of hydrodynamic interactions and the free energy profile are found to be highly correlated with the behavior of water molecules in the interplate region, in agreement with our prior work.[22]

We presently consider three types of graphene-like plates: plates with a "fully" attractive solute−solvent interaction potential, plates with a "reduced" attractive solute−solvent potential, and plates with a purely repulsive solute−solvent potential. For the plates with either a reduced attractive potential or a purely repulsive potential, capillary evaporation occurs when the interplate separation is smaller than a critical value. In contrast, capillary evaporation does not occur for plates with a fully attractive solute−solvent potential. As the fully attractive plates approach each other, we observe solvent layering with water molecules being eventually expelled from the interplate region due to steric repulsion. Both dewetting in the former cases and solvent layering in the latter case greatly affect the solvent fluctuations in the interplate region and give rise to molecular scale effects in the hydrodynamic interactions. We compute the spatial dependence of the friction tensor and investigate the relation between the static and dynamic fluctuations of water density in the interplate region and this property.

Given the potential of mean force and position-dependent friction coefficient, we compute the rate of diffusion-controlled association by means of Brownian dynamics (BD) simulations. The predictions of BD are tested against the results garnered from a set of molecular dynamics (MD) simulations of assembly in explicit solvent. This serves as a test of the validity of the Markovian approximation inherent in Brownian dynamics simulation and the ability of coarse-grained stochastic dynamics to adequately capture the kinetic effects associated with the bath. We find that there is reasonable agreement between the two simulations when molecular-scale hydrodynamic interactions are included in the BD but marked disagreement when hydrodynamic interactions are neglected. The observation that BD with hydrodynamic interactions is in agreement with the MD result is somewhat surprising since, as we show, slow solvent fluctuations play an important role in the assembly process, and we would thus expect non-Markovian

effects to be of importance. The agreement between BD and MD indicates that the non-Markovian effects may be encoded in the spatial dependence of the friction coefficient in an average way.

2. SYSTEM AND METHOD

We modeled the hydrophobic plate as a graphene-like sheet with an area of (1.2×1.3) nm^2 as shown in Figure 1. The plate size was chosen to facilitate both nanometer-scale drying transitions and comparison with our prior work on nanospheres. To vary the hydrophobicity, we studied three types of plates, all with a carbon−carbon bond length of 0.145 nm and a Lennard-Jones diameter of $\sigma_{CC} = 0.35$ nm but with different interaction potential well depths: (a) full Lennard-Jones (LJ) interaction with $\varepsilon_{CC} = 0.276$ kJ/mol,[29] (b) reduced LJ interaction with $\varepsilon_{CC} = 0.055$ kJ/mol, and (c) purely repulsive Weeks−Chandler−Anderson (WCA) truncation of the full LJ potential.[30] For convenience, these three types of plates are denoted as (full) LJ plates, reduced LJ plates, and WCA plates in the present work. Solute−solvent interactions are given by the geometric mean of the respective water and solute parameters.

To calculate the relative friction coefficient, two parallel plates are placed perpendicular to the z-axis. A series of simulations are run with the plates fixed at various separations, and all internal degrees of freedom are frozen. The interplate separation ranges from 0.4 to 2 nm (for the full and reduced LJ plates) or to 2.2 nm (for the WCA plates). The solvent-induced mean force is computed from such fixed configurations, although a finer grid spacing in z is employed. To obtain the potential of mean force (PMF), this quantity is then integrated in combination with the direct plate−plate interactions.

In the simulations of the association process, two plates are initially placed ≈1.8 nm apart. The lower plate is fixed to its position, and a biased force along the −z direction is applied to the upper plate. Harmonic potentials are utilized to treat the intramolecular stretches ($k_b = 392721.8$ kJ/mol nm^{-2} and $d_0 = 0.14$ nm) and bends ($k_\theta = 5271.84$ kJ/mol rad^{-2} and $\theta = 120°$). Snapshots from the association of reduced LJ plates and representative trajectories plotted along the reaction coordinate are shown in Figure 1. The results from these two sets of

calculations are discussed in Section 4.2 and Section 4.3, respectively. In addition, we determine the friction coefficient on a single plate, in a system containing only one plate, by pulling it at a constant speed perpendicular to its plane and computing the drag force along its normal direction.

All systems are solvated by TIP4P water.[31] The size of the solvation box of the full LJ and reduced LJ system is $4 \times 4 \times 4$ nm^3, and for the WCA system the box size is increased to $5 \times 5 \times 6$ nm^3. This is done to accommodate the large volume fluctuation that arises from the strong dewetting transition.

In the calculation of the friction, each system is equilibrated with a 2 ns isothermal-isobaric (NPT) simulation ($P = 1$ atm, $T = 300$ K). The Berendsen method[32] and the stochastic velocity rescaling method[33] are chosen for the barostat and thermostat, respectively. For each system, there are 12−18 microcanonical (NVE) production runs of 4 ns to compute the friction coefficient. To facilitate energy conservation, double precision routines are utilized for all NVE runs. To study the dragging force of the single plate, we choose four pulling rates ranging from 0.5 to 3 nm/ns. There are at least 12 NPT runs for each pulling rate that are utilized to obtain an accurate estimate of dragging force. We perform at least 55 runs with various initial configurations for each system to fully characterize the association process of two plates and estimate the distribution of mean passage times. All simulations are performed using GROMACS 4.5.3, and the Particle-Mesh Ewald technique is utilized to treat long-range electrostatics.[34,35]

3. BROWNIAN DYNAMICS WITH HYDRODYNAMIC INTERACTIONS

Within the framework of Brownian dynamics, hydrodynamic interactions are encoded in the frictional force. The stochastic equation for the association process contains contributions from the mean force, the frictional force, and the Gaussian random force. The potential of mean force, $W(z)$, includes the contributions from the direct plate−plate interaction and the solvent-induced interaction. The separation between two plates, z, is treated as the reaction coordinate. Hydrodynamic interactions give rise to the spatial dependence of the relative friction coefficient, $\zeta(z)$, and through this the spatially dependent diffusion coefficient $D(z) = kT/\zeta(z)$.

The stochastic BD equation for plate association can be therefore written as[36]

$$\dot{z} = -\beta D(z)\frac{\partial}{\partial z}W(z) + \frac{\partial}{\partial z}D(z) + R(z, t) \qquad (1)$$

where $\beta \equiv 1/k_B T$ and the diffusion coefficient is related to the "random force" $R(z,t)$ through the fluctuation-dissipation theorem

$$\langle R(t')R(t)\rangle = 2D(z)\delta(t - t') \qquad (2)$$

This equation of motion is an accurate description of the dynamics in the high friction limit for time scales greater than the momentum relaxation time and in which the solvent time scale is fast compared to the time scale for the motion of the heavy bodies. The dynamics can alternatively be expressed as a Smoluchowski equation for the probability distribution $P(z,t)$ of finding the particle at z at time t

$$\frac{\partial P(z, t)}{\partial t} = \frac{\partial}{\partial z}D(z)\left(\frac{\partial}{\partial z} + \beta W'(z)\right)P(z, t) \qquad (3)$$

This equation or BD can be used to determine mean first passage times for diffusion-controlled reactions once $W(z)$ and $\zeta(z)$ are known.

To apply BD we must determine the PMF and spatial dependence of the friction coefficient along the reaction path. As already pointed out, the continuum treatment of the hydrodynamic interaction breaks down at small separations.[20−22] In this work, we calculate the friction coefficient on the molecular length scale from explicit molecular dynamics simulations. The friction coefficient can then be determined from the two-body friction tensor ζ_{ij}. In the calculation, the plates are fixed as required in the Brownian limit. The pair friction tensor can be expressed as a time integral of the correlation functions of the fluctuating force $\delta\vec{F}_i = \vec{F}_i - \langle\vec{F}_i\rangle$,

$$\zeta_{ij} = \beta \int_0^\infty dt \lim_{n\to\infty} \langle\delta\vec{F}_i(t)\delta\vec{F}_j(0)\rangle \qquad (4)$$

where by symmetry $\zeta_{12} = \zeta_{21}$ and $\zeta_{11} = \zeta_{22}$. Here we focus on the direction parallel to the interplate separation and therefore study the force components along the plate normal vector. Equation 4 is only valid in the limit where the number of solvent molecules, n, approaches infinity.[28] In the present case of finite systems, it is still possible to relate the force autocorrelation function to the friction tensor, following the procedure of Bocquet et al.[28] The friction along the relative coordinate is given by $(\zeta_{11} - \zeta_{12})/2$ and depicted in Section 4.2.

4. RESULTS

4.1. Friction and Diffusion Coefficients of a Single Plate. The friction coefficient perpendicular to the face of a single plate immersed in solvent may be extracted from the force autocorrelation function by means of techniques outlined in ref 37. The resultant calculation yields values of 1.63×10^{-11}, 1.33×10^{-11}, and 1.0×10^{-11} kg/s, when the solvent−solute interaction is the full LJ, reduced LJ, and the WCA potential, respectively. In agreement with prior work,[22] the friction experienced by the body decreases with increasing surface hydrophobicity. Each calculation is performed in a periodic box of dimensions given in Section 2.

The friction coefficient may also be extracted from a set of nonequilibrium simulations where the plate is dragged through the solvent at a given velocity. As depicted in Figure 2, the dragging force at four velocities is determined from MD simulations in explicit solvent and grows with increasing velocity. The resultant plot of dragging force versus pulling rate exhibits a linear relationship with the slope equal to the friction coefficient. The extracted values of the friction are given in Table 1, alongside the results computed from the force autocorrelation function. The two estimates of the friction are in close agreement. The consistency between the results garnered from two different techniques serves to validate the calculation.

Next, we compare these results to the predictions of continuum hydrodynamics. The friction coefficient for a rigid body described by a set of spherical sites can be evaluated by means of the Rotne−Prager tensor.[38] The translational friction coefficient may be extracted from the full $3N \times 3N$ mobility tensor, where N is the number of sites.[39] In the present calculation, periodic boundary conditions must be taken into account and are known to have a significant impact on hydrodynamic properties.[40−42] Periodic effects may be treated by means of replacing the standard Rotne−Prager tensor with a
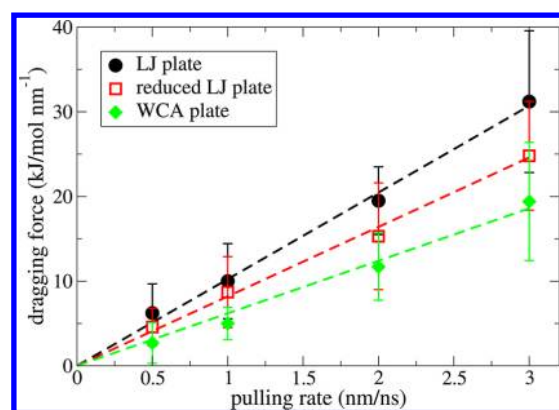
Figure 2. Dragging force of a single plate moving at constant velocity. The results for the plate with full Lennard-Jones (LJ) interaction (LJ plate), the plate with reduced LJ interaction (reduced LJ plate), and purely repulsive Weeks−Chandler−Anderson truncation of the full LJ potential (WCA plate) are depicted in black, red, and green, respectively. The dragging forces increase linearly as the pulling rate increases, and the fitted slopes are equal to the friction coefficient.

Table 1. Friction on a Single Plate in the z-Direction, As Estimated from the Force Autocorrelation Function, Pulling Simulations, and Continuum Hydrodynamics

interaction	box (nm^3)	ζ_{FACF} (10^{-11} kg/s)	ζ_{PULL} (10^{-11} kg/s)	ζ_{STICK} (10^{-11} kg/s)
WCA	$5 \times 5 \times 6$	1.00	1.03	1.27
REDUCED	$4 \times 4 \times 4$	1.33	1.36	1.53
FULL	$4 \times 4 \times 4$	1.63	1.69	1.53

form that accounts for periodicity via an Ewald summation.[41] This approach is discussed further in the Appendix.

As discussed above, different solvation boxes are utilized in the WCA and Lennard-Jones systems, and the continuum calculation must be undertaken for both sizes. The values of the friction coefficient with stick boundary conditions for the two box sizes are given in Table 1. The full LJ value is somewhat larger than the continuum result, whereas in line with expectations, the increasingly hydrophobic plates begin to show larger deviations from the stick boundary condition.

4.2. Hydrodynamic and Thermodynamic Profiles. Friction coefficients, $\zeta(z)$, and the potential of mean force, $W(z)$, are depicted as a function of interplate separation, z, in Figures 3, 4, and 5 (for the full LJ, reduced LJ, and WCA plate, respectively). The frictional profiles exhibit nonmonotonic behavior as the two plates approach each other. The spatially dependent features of the molecular scale hydrodynamic interactions display trends similar to those found in the free energy profile. This finding is in agreement with our previous work[22] and the recent work of Mittal and Hummer.[43] In the case of the full LJ plate, the friction peaks and the free energy increases as a layer of water is "squeezed out"[9] at $z = 0.88$ nm. The friction coefficient subsequently decreases at the minimum of the PMF. The final solvent layer is expelled as the separation decreases to 0.62 nm, and both the free energy and the friction coefficient increase. It is important to note that the friction profile peaks at 0.88 and 0.62 nm, which are at the same positions as the PMF barriers. The peak heights at these two separations are 23.3(4.2) × 10^{-10} and 4.0(0.4) × 10^{-10} kg/s, respectively. Standard errors of the mean value are given in parentheses.
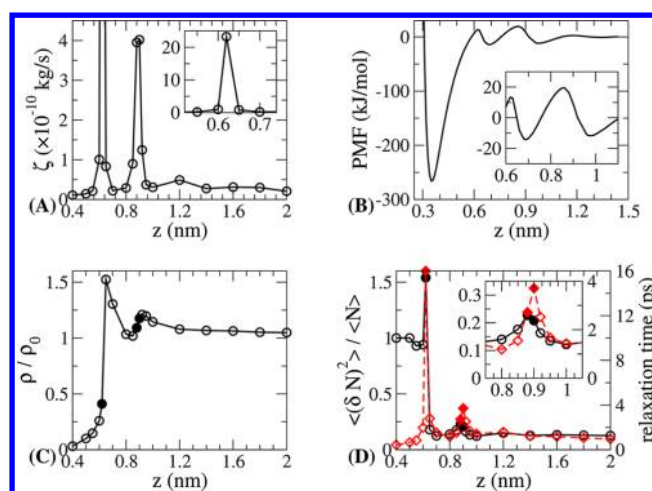

Figure 3. Spatial dependence of relative friction coefficient (A) and the potential of mean force (B) for the association of two LJ plates. The friction peaks at $z = 0.62$ nm and two free energy wells at $z = 0.68$ and 0.97 nm are depicted in the insets of (A) and (B), respectively. (C) The relative density of water in the interplate region. (D) The ratio of the variance to the average of the number of water molecules (black) and the solvent relaxation time in the interplate region (red). For both curves in (D), the peaks at $z \approx 0.9$ nm are depicted in the inset. The values corresponding to the friction peaks are shown as filled symbols in panels (C) and (D).
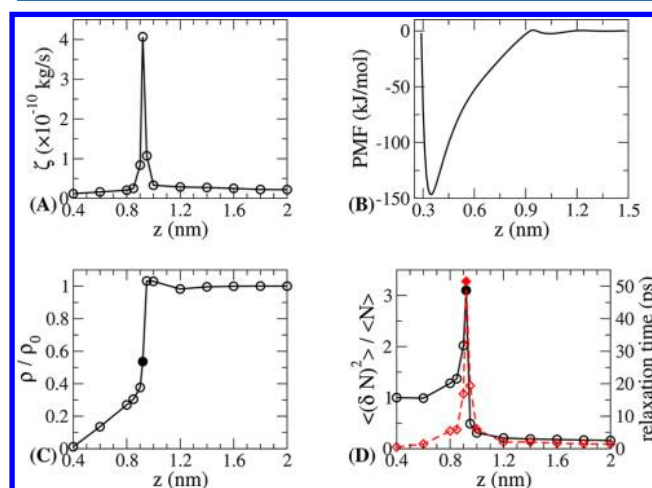

Figure 4. Spatial dependence of relative friction coefficient (A) and the potential of mean force (B) for the association of two reduced LJ plates. (C) The relative density of water in the interplate region. (D) The ratio of the variance to the average of the number of water molecules (black) and the solvent relaxation time in the interplate region (red). The value corresponding to the friction peak is shown as filled symbols in panels (C) and (D).

For the reduced LJ plates, there is a low barrier at $z = 0.9$ nm in the PMF, whereas the WCA plates exhibit barrierless assembly along the chosen reaction coordinate. In these cases, the corresponding friction profiles also display nonmonotonic behavior. The friction profile peaks at $z_c = 0.92$ nm and $z_c = 1.35$ nm for the reduced LJ and WCA plates, respectively. As discussed below, these distances are in the region of the critical separation for dewetting. The corresponding peak heights of the friction coefficients are 4.1(0.85) × 10^{-10} (reduced LJ) and 2.2(0.61) × 10^{-10} kg/s (WCA). The somewhat large error bar results from the sizable force fluctuations that are present in the vicinity of z_c.
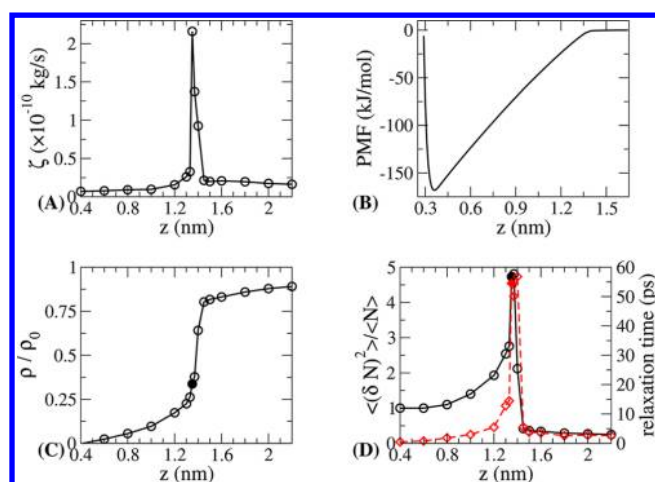
Figure 5. Spatial dependence of relative friction coefficient (A) and the potential of mean force (B) for the association of two WCA plates. (C) The relative density of water in the interplate region. (D) The ratio of the variance to the average of the number of water molecules (black) and the solvent relaxation time in the interplate region (red). The value corresponding to the friction peak is shown as filled symbols in panels (C) and (D).

The friction profiles converge to 2.1×10^{-11} (LJ), 2.2×10^{-11} (reduced LJ), and 1.6×10^{-11} (WCA) kg/s at large separations. The standard error in the mean for these values is $\approx 10\%$. These numbers are somewhat larger than expected upon comparison with the results given in Table 1. This difference may largely result from the finite box size and the impact of neighboring periodic images. However, the effect of periodic boundary conditions should not greatly impact the observed spatial dependence of the short-range hydrodynamics interactions.

To better understand the nature of molecular-scale hydrodynamic interactions, we analyze the density and the static and dynamic fluctuations in number of water molecules in the interplate region. The static fluctuations are measured by the ratio of the number variance to the average $\langle(\delta N)^2\rangle/\langle N\rangle$. An estimate of the solvent relaxation time can be computed from the integral of the normalized autocorrelation function of these fluctuations, $\langle \delta N(t)\delta N(0)\rangle/\langle(\delta N)^2\rangle$. The resultant plots of these quantities as a function of interplate separation are depicted in Figures 3–5. Additionally, the values of the solvent density and fluctuations at the separation that correspond to the maximum friction are marked on the curves. For the LJ plates, the solvent density decreases when the plate separation decreases from 0.9 to 0.85 nm. The ratio of the variance to the average of water density peaks at $z = 0.88$ nm, and the relaxation time peaks at $z = 0.90$ nm. Both peaks occur at separations close to where the friction coefficient peaks. Moreover, when the separation decreases from 0.65 to 0.62 nm, the solvent density sharply decreases. The static fluctuations and relaxation time grow in the process of water expulsion. Both the static variance of water density and the relaxation time peak at the same separation where the friction coefficient peaks ($z_c = 0.62$ nm).

In both the reduced LJ and WCA systems, the solvent density in the interplate region begins to decrease at the critical separation of the dewetting transition. For the reduced LJ plate, the solvent density dramatically decreases when the separation decreases from 0.95 to 0.92 nm. Both the variance of water density and the solvent relaxation time peak at $z_c = 0.92$ nm.

The density of water between the WCA plates decreases as the separation decreases from 1.45 to 1.35 nm. The ratio of the variance to the average of water density and the solvent relaxation time peak in the same region. At the critical separation for the dewetting transition, the interplate region fluctuates between wet and dry. The value of the critical distance between surfaces is on the order of 1 nm for the present-sized plates and decreases with decreasing hydrophobicity, in agreement with macroscopic thermodynamic analysis.[6,15,44] This characterization of the density and the fluctuation of solvent is consistent with the results of previous studies.[6,22]

In the three systems presently studied, it can be clearly seen that the friction coefficient increases where the solvent fluctuations become large and slow. Taken together, both static and dynamic solvent behavior engender the large frictions at small interplate separations. In agreement with our prior work,[22] molecular-scale hydrodynamic interactions largely result from such fluctuations when, in the case of hydrophobic bodies, the drying transition occurs or, for less hydrophobic species, when water molecules are expelled from the interplate region due to steric repulsion.

4.3. Comparison of Brownian Dynamics with Molecular Dynamics. To further elucidate the impact of molecular-scale hydrodynamics on the kinetics of self-assembly, we perform direct molecular dynamics simulations of this process. The two plates are initially placed perpendicular to the z-direction at a separation of ~1.8 nm. A constant loading force is added to the upper plate, and the lower plate is fixed in its initial position. The loading force utilized is 440 pN (full LJ) or 20 pN (reduced LJ and WCA). There are at least 55 association simulations performed for each system.

The assembly of both the WCA plates and reduced LJ plates slows down around the critical separation for dewetting. This process is illustrated for the reduced LJ case by the sample trajectories depicted in Figure 1.[45] One can see there is a large dwell time at $z \approx 1$ nm. In the case of the full LJ system, the upper plate initially rapidly approaches the lower plate, and the interplate distance decreases to $z = 0.95$ nm, corresponding to two interplate water layers. The association process then stagnates. After some period a water layer is expelled, and the plate separation decreases to $z = 0.66$ nm where a single water layer separates the plates. There is another dwell time before the last water layer is expelled, and the two plates finally come into contact. During the association process the upper plate can rock. This is particularly pronounced around $z = 0.66$ nm where the amplitude of the rocking can be as much as 0.2 nm. To provide the best comparison with the (one-dimensional) BD scheme outlined below, the plates must be kept as parallel as possible. This is facilitated by the addition of a harmonic restraining potential on the plate's internal degrees of freedom. It is important to note that outside the present context "rocking" could be a viable degree of freedom, and we observe that assembly occurs significantly more rapidly when such effects are included. In the case of less attractive or purely repulsive solvent–solute interactions, the effect is much less prominent, as the displacement generated by the rocking mode is small with respect to the critical separation for dewetting that drives assembly (≈ 1 nm).

As we will show, the mean first passage times observed in the MD association trajectories cannot be predicted by solely considering the free energy profile with constant friction. To evaluate the role of hydrodynamic interactions in assembly, we

utilize a one-dimensional Brownian dynamics (BD) scheme as described in Section 3, where the system evolves according to eq 1 and can be integrated as described by Ermak and McCammon.[16] The dynamical degree of freedom is taken to be the interplate distance, z, along which the friction and potential of mean force have been computed (see Figures 3−5).

This scheme may be utilized to generate predictions for the mean first passage time (mfpt) and distribution of first passage times (dfpt) from BD simulations with the loading force. Such a comparison serves to evaluate the degree to which the Brownian framework can yield an adequate description of the kinetics of assembly. The constant force F_0 applied to the molecular dynamics simulations is accounted in the BD by a means of the modified potential of mean force $U(z)$

$$U(z) = W(z) + F_0 z \qquad (5)$$

where $W(z)$ is the PMF determined from MD in the absence of a loading force. Because the loading force F_0 in eq 5 is independent of the solution degrees of freedom, eq 5 is rigorous. Moreover, because the loading potential is linear in z, we assume it will not alter the spatial dependence of the friction. However, for very large loading forces, we expect that nonequilibrium effects will be significant, and the BD picture will fail. For each system, we have generated 10 000 BD trajectories given initial state z_0 and an absorbing boundary at z_A. For each system, the values of these parameters and of the mean first passage time are given in Table 2. The

Table 2. Mean First Passage Time, $\bar{\tau}$, of the Plate Association Process As Described in Section 4.3

type	F_0 (pN)	$\bar{\tau}_{MD}$ (ps)	$\bar{\tau}_{BD-HI}$ (ps)	$\bar{\tau}_{BD-NOHI}$ (ps)	z_0 (nm)	z_A (nm)
WCA	20	515	516	134	1.60	0.40
reduced LJ	20	1469	2390	200	1.20	0.40
LJ (first barrier)	440	573	1460	85	1.20	0.80
LJ (second barrier)	440	32600	23078	243	0.75	0.40

corresponding first passage time distributions are shown in Figure 6. The mean first passage time may also be computed directly from the Smoluchowski Equation (eq 3) by means of the following expression[46]

$$\bar{\tau}(z_0) = \beta \int_{z_0}^{z_A} dy \, \frac{\zeta(y)}{e^{-\beta U(y)}} \int_{z_R}^{y} dx e^{-\beta U(x)} \qquad (6)$$

where $\beta \equiv 1/k_B T$ and z_R is the positon of the reflecting boundary. Due to the driving force, the reflecting boundary can be taken to large values in our calculation. This equation and an ensemble of BD trajectories will yield the same result within numerical error.

The mean first passage time obtained from MD simulation for the association of the reduced LJ plates is about 60% smaller than the result from BD simulation with hydrodynamic interactions (BD with HI) but 7 times larger than the value estimated from BD when the spatial dependence of the friction is not included and the single plate friction (see Table 1) is utilized instead (BD without HI). The fpt distribution obtained from MD is also close to, albeit narrower than, that obtained from BD with HI. In contrast, the distribution garnered from BD without HI is much more strongly peaked. In the case of the WCA plates, the mfpt and the fpt distribution from both
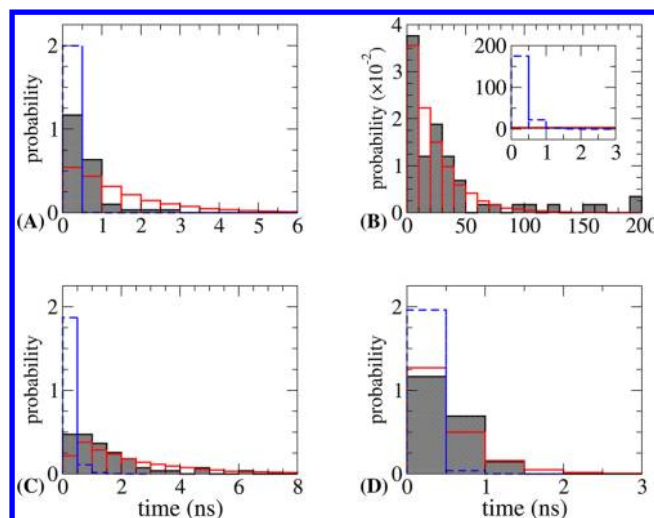

Figure 6. Distribution of first passage time (dfpt) for the association process of LJ plates (panel (A), first barrier; panel (B), second barrier), reduced LJ plates (C), and WCA plates (D), obtained from the MD simulation (black) and BD simulation with and without the consideration of hydrodynamic interactions (HI) (red and blue, respectively). The dfpt's obtained from MD are in reasonable agreement with the result of BD with HI, and the probability of having a fpt smaller than 500 ps is much larger in the results garnered by BD without HI.

MD and BD with HI are very close to each other, but both are approximately 4 times larger than the BD without HI result.

The results of MD simulation are in reasonable agreement with those obtained from BD with HI for both the WCA and the reduced LJ plate systems. The association process slows down in the region around the critical separation for the dewetting transition where the friction peaks. As discussed above, the behavior of friction profile at the critical separation largely results from the solvent fluctuation due to the dewetting transition. The molecular-scale effect of hydrodynamic interactions evidently contributes to the slowing down of the association process near the critical separation, and if only barriers present in the PMF are considered (as in BD without HI), association occurs far too rapidly. These results indicate that a kinetic barrier along the reaction coordinate is present at the drying transition.

The values of the mfpt of the first (second) barrier of the full LJ plate system as obtained from BD with HI are 1460 (23 078) ps, much larger than the results of 85 (243) ps for BD without HI. Hydrodynamic interactions strikingly slow down the first passage time over the second barrier by about 2 orders of magnitude. The mfpt obtained from the MD simulation is 573 and 32 600 ps, for the first and second barrier, respectively. For the first barrier, the mfpt obtained from MD simulations is smaller than the result from BD with HI while still being much larger than the result from BD without HI. Meanwhile, for the second barrier, the mean first passage time from MD simulations is larger than the result from BD simulations with HI. The distribution of the first passage times corresponding to the second barrier obtained from MD simulations is similar to the results from BD simulations with HI. For passage over the first barrier, the distributions exhibit greater deviation.

In general, the average value and the distribution of mean first passage times of the three types of plates calculated from MD simulations is consistent with the results of BD simulations with HI. In prior work,[22] we found that hydrodynamic

interactions contributed approximately 40% to the assembly of two fullerenes. In the present set of calculations, hydrodynamic interactions contribute a much larger share. Comparison of spheres and plates indicates that the contribution of the hydrodynamic interaction is enhanced as the shape is flattened. More water molecules are confined by plates than spheres of the same surface area so that, at small separations, the degree of confinement and the length scale of dewetting are increased.

5. CONCLUSION

In this work, we study the impact of hydrodynamic effects on the kinetics of assembly of two plates of varying hydrophobicity. To this end, the potential of mean force and spatially dependent friction coefficient are determined along the interplate separation. The results show that there is a correspondence between peaks in the PMF and peaks in the frictional profile. High values of the friction are related to large and slow solvent fluctuations in the interplate region. Both solvent confinement and drying phenomena can play a critical role in the kinetics of assembly. In this way, molecular-scale effects shape the hydrodynamic interactions and give rise to their deviation from continuum theory, which predicts that the friction coefficient diverges as two bodies come into contact.[47,48]

The kinetics of assembly studied by means of molecular dynamics simulations in explicit solvent with a constant loading force applied along the reaction coordinate is compared with the predictions of Brownian dynamics with the same loading force and with the potential of mean force and hydrodynamic profile extracted from the data presented in Section 4.2. Brownian dynamics is a widely used technique owing to its computational efficiency as solvent degrees of freedom are not treated explicitly. There is reasonable agreement between the mean first passage times that are obtained from the two schemes. Indeed, we find that hydrodynamic interactions are essential to produce a reasonable description of the process, and neglect of spatial dependence of the friction has a large impact on the kinetics. The HI give rise to kinetic bottlenecks along the association pathway,[22] over and above the barriers in the potential of mean force. Interestingly, other degrees of freedom such as plate "rocking" can in some cases significantly increase the rate of assembly, probably by facilitating the entry and exit of water from the interplate gap. To describe the effect of solvent relaxation on the rocking mode within the Brownian framework, it would require a determination of the friction coefficient experienced on this degree of freedom. The exploration of all possible pathways to plate assembly is beyond the scope of this work, and presently we concentrate on the approach of two parallel plates.

It has been suggested[6,7] that including solvent degrees of freedom in the reaction coordinate is necessary to properly characterize the association process. Presently, a reaction coordinate is utilized that is only a function of the plate degrees of freedom. We have shown that such a choice is reasonable provided that (molecular-scale) hydrodynamic interactions are considered along the pathway. The inclusion of hydrodynamic effects captures the effect of solvent in an average sense, and the Brownian framework would be an exact treatment in the limit where the solvent time scales are much faster than those associated with the heavy bodies. Leading from the last point, the discrepancies between the MD and BD results can be largely attributed either to the impact of the pulling force—that is, the friction experienced along the force-biased surface significantly differs from that extracted from the equilibrium calculations—or to non-Markovian effects. In the case of the passage over the first barrier of the LJ system, at least some of the deviation is likely due to the large pulling force, although non-Markovian effects should have an impact both in this case and in the other system studied. It has, for instance, been shown that dynamical caging effects can be exhibited along degrees of freedom that are associated with slowly varying memory functions.[49] Such phenomena can also serve to explain the long dwell times exhibited in the association trajectories.

Unfortunately, given the broad distributions involved and limited number of MD trajectories that can be harvested, it is difficult to fully gauge the impact of non-Markovian effects based on the present work. Certainly, it is observed that, in the case of strongly hydrophobic plates, assembly is almost always preceded by the "first" drying transition; that is, the system does not sample successive wet and dry states near the critical separation. One should expect such a process to be intrinsically non-Markovian, although the BD with HI approach that is presently employed appears to at least capture some aspect of this "waiting period" for drying in an average way. A more precise understanding of this phenomena will be the subject of future work.

■ APPENDIX: CONTINUUM HYDRODYNAMIC TREATMENT OF THE FRICTION ON A RIGID BODY

Consider a rigid body made up of N spherical sites where the origin is taken to be the center of mass. A $3N \times 3N$ mobility tensor $\underline{B}$ may be defined where

$$\mathbf{V} = \underline{B} \bullet \mathbf{F} \tag{7}$$

and where $\mathbf{V}$ and $\mathbf{F}$ are $3N$ dimensional vectors representing the velocities and external forces on the N sites that comprise the body. In the case of stick boundary conditions, the elements of $\underline{B}$ are approximated by the Rotne−Prager tensor[38] where the 3 × 3 elements, $\underline{B}_{ij}$, are given as

$$\underline{B}_{ij} = \frac{1}{6\pi\eta a}[\delta_{ij} + (1 - \delta_{ij})\underline{T}_{ij}] \tag{8}$$

where a is the site radius and η is the shear viscosity. For TIP4P water, the value is $\eta = 0.494$ mPa s and has been taken from the literature.[50] The matrix $\underline{T}_{ij}$ is given by the following expression

$$\underline{T}_{ij} = \begin{cases} \dfrac{3}{4}\dfrac{a}{r_{ij}}(\underline{I} + \hat{\hat{r}}\hat{r}_{ij}) + \dfrac{1}{2}\left(\dfrac{a}{r_{ij}}\right)^3(\underline{I} - 3\hat{\hat{r}}\hat{r}_{ij}) & r_{ij} > 2a \\[3mm] \left(1 - \dfrac{9}{32}\dfrac{r_{ij}}{a}\right)\underline{I} + \left(\dfrac{3}{32}\dfrac{r_{ij}}{a}\right)\hat{\hat{r}}\hat{r}_{ij} & r_{ij} \leq 2a \end{cases} \tag{9}$$

where $r_{ij} = |\vec{r}_{ij}|$ and $\hat{\hat{r}}\hat{r}_{ij}$ is the vector direct product of the unit vector of displacement. If the plate is treated as a body that is centro- and axisymmetric, then the translational friction tensor, $\underline{\zeta}_T$, is given by the following expression[39]

$$\underline{\zeta}_T = \sum_{ij}[\underline{B}^{-1}]_{ij} \tag{10}$$

where $\underline{\zeta}_T$ is a diagonal 3 × 3 matrix. Presently, we are interested in the friction coefficient associated with motion perpendicular to the face of the plates, and this is what is

reported in Section 4.1. For periodic systems, the elements of $\underline{\underline{B}}$ are given by

$$\underline{\underline{B}}_{ij}^{\text{pbc}} = \sum_{\vec{n}} \underline{\underline{B}}_{ij}^{\vec{n}} \tag{11}$$

where $\vec{n}$ is the periodic image vector and $B_{ij}^{\vec{n}}$ the same as in eq 8 except it is evaluated over periodic images. This expression may be evaluated by means of an Ewald summation, as was shown by Beenakker.[41] In the case of overlapping spheres, reciprocal space contributions are excluded from the Ewald sum, as the long-range portion of the hydrodynamic interaction only includes terms for which $r_{ij} > 2a$.

■ AUTHOR INFORMATION

Corresponding Author
*E-mail: bb8@columbia.edu.

Notes
The authors declare no competing financial interest.

■ ACKNOWLEDGMENTS

■ REFERENCES

(1) Berne, B. J.; Weeks, J. D.; Zhou, R. *Annu. Rev. Phys. Chem.* **2009**, *60*, 85−103.
(2) Wallqvist, A.; Berne, B. J. *J. Phys. Chem.* **1995**, *99*, 2893−2899.
(3) Chandler, D. *Nature* **2005**, *437*, 640−647.
(4) Lum, K.; Chandler, D.; Weeks, J. *J. Phys. Chem. B* **1999**, *103*, 4570−4577.
(5) Jamadagni, S. N.; Godawat, R.; Garde, S. *Annu. Rev. Chem. Biomol. Eng.* **2011**, *2*, 147−171.
(6) Huang, X.; Margulis, C. J.; Berne, B. J. *Proc. Natl. Acad. Sci. U.S.A.* **2003**, *100*, 11953−11958.
(7) Willard, A. P.; Chandler, D. *J. Phys. Chem. B* **2008**, *112*, 6187−6192.
(8) Patel, A. J.; Varilly, P.; Chandler, D. *J. Phys. Chem. B* **2010**, *114*, 1632−1637.
(9) Zangi, R. *J. Phys. Chem. B* **2011**, *115*, 2303−2311.
(10) Zhou, R.; Huang, X.; Margulis, C. J.; Berne, B. J. *Science* **2004**, *305*, 1605−1609.
(11) Liu, P.; Huang, X.; Zhou, R.; Berne, B. J. *Nature* **2005**, *437*, 159−162.
(12) Bolhuis, P. G.; Chandler, D. *J. Chem. Phys.* **2000**, *113*, 8154−8160.
(13) Leung, K.; Luzar, A.; Bratko, D. *Phys. Rev. Lett.* **2003**, *90*, 065502.
(14) Luzar, A. *J. Phys. Chem. B* **2004**, *108*, 19859−19866.
(15) Sharma, S.; Debenedetti, P. G. *Proc. Natl. Acad. Sci. U.S.A.* **2012**, *109*, 4365−4370.
(16) Ermak, D. L.; McCammon, J. A. *J. Chem. Phys.* **1978**, *69*, 1352−1360.
(17) Ando, T.; Skolnick, J. *Proc. Natl. Acad. Sci.* **2010**, *107*, 18457−18462.
(18) Brady, J. *Annu. Rev. Fluid Mech.* **1988**, *20*, 111−157.
(19) Brady, J. F.; Philips, R. J.; Lester, J. C.; Bossis, G. *J. Fluid Mech.* **1988**, *195*, 257−280.
(20) Thomas, J. A.; McGaughey, A. J. H. *Phys. Rev. Lett.* **2009**, *102*, 184502.
(21) Bocquet, L.; Charlaix, E. *Chem. Soc. Rev.* **2010**, *39*, 1073−1095.
(22) Morrone, J. A.; Li, J.; Berne, B. J. *J. Phys. Chem. B* **2012**, *116*, 378−389.
(23) Giovambattista, N.; Debenedetti, P. G.; Rossky, P. J. *J. Phys. Chem. C* **2007**, *111*, 1323−1332.
(24) Rasaiah, J. C.; Garde, S.; Hummer, G. *Annu. Rev. Phys. Chem.* **2008**, *59*, 713−740.
(25) Baron, R.; Setny, P.; McCammon, J. A. *J. Am. Chem. Soc.* **2010**, *132*, 12091−12097.
(26) Li, J.; Liu, T.; Li, X.; Ye, L.; Chen, H.; Fang, H.; Wu, Z.; Zhou, R. *J. Phys. Chem. B* **2005**, *109*, 13639−13648.
(27) Harada, R.; Sugita, Y.; Feig, M. *J. Am. Chem. Soc.* **2012**, *134*, 4842−4849.
(28) Bocquet, L.; Hansen, J.; Piasecki, J. *J. Stat. Phys.* **1997**, *89*, 321−346.
(29) Werder, T.; Walther, J.; Jaffe, R.; Halicioglu, T.; Koumoutsakos, P. *J. Phys. Chem. B* **2003**, *107*, 1345−1352.
(30) Weeks, J. D.; Chandler, D.; Andersen, H. C. *J. Chem. Phys.* **1971**, *54*, 5237−5247.
(31) Jorgensen, W. L.; Madura, J. D. *J. Chem. Phys.* **1985**, *56*, 1381−1392.
(32) Berendsen, H. J. C.; Postma, J. P. M.; van Gunsteren, W. F.; DiNola, A.; Haak, J. R. *J. Chem. Phys.* **1984**, *81*, 3684−3690.
(33) Bussi, G.; Donadio, D.; Parrinello, M. *J. Chem. Phys.* **2007**, *126*, 014101.
(34) Darden, T.; York, D.; Pedersen, L. *J. Chem. Phys.* **1993**, *98*, 10089−10092.
(35) Hess, B.; Kutzner, C.; van der Spoel, D. *J. Chem. Theory Comput.* **2008**, *4*, 435−447.
(36) Tough, R. J. A.; Pusey, P. N.; Lekkerkerker, H. N. W.; Broeck, C. V. D. *Mol. Phys.* **1986**, *59*, 595−619.
(37) Bocquet, L.; Hansen, J.; Piasecki, J. *J. Stat. Phys.* **1994**, *76*, 527−548.
(38) Rotne, J.; Prager, S. *J. Chem. Phys.* **1969**, *50*, 4831−4837.
(39) Carrasco, B.; de la Torre, J. G. *Biophys. J.* **1999**, *75*, 3044−3057.
(40) Hasimoto, H. *J. Fluid Mech.* **1959**, *5*, 317−328.
(41) Beenakker, C. *J. Chem. Phys.* **1986**, *85*, 1581−1582.
(42) Yeh, I. C.; Hummer, G. *J. Phys. Chem. B* **2004**, *108*, 15873−15879.
(43) Mittal, J.; Hummer, G. *J. Chem. Phys.* **2012**, *137*, 034110.
(44) Lum, K.; Luzar, A. *Phys. Rev. E* **1997**, *56*, R6283−R6286.
(45) Humphrey, W.; Dalke, A.; Schulten, K. *J. Mol. Graphics* **1996**, *14*, 33−38.
(46) Zwanzig, R. *Nonequilibrium Statistical Mechanics*; Oxford University Press: New York, 2001.
(47) Wolynes, P. G.; Deutch, J. M. *J. Chem. Phys.* **1976**, *65*, 450−454.
(48) Jeffrey, D. J.; Onishi, Y. *J. Fluid Mech.* **1984**, *139*, 261−290.
(49) Tuckerman, M. E. *Statisical Mechanics: Theory and Molecular Simulation*; Oxford University Press: New York, 2010.
(50) Gonzalez, M. A.; Abascale, J. F. *J. Chem. Phys.* **2010**, *132*, 096101.